Materials Advances

ROYAL SOCIETY OF CHEMISTRY

PAPER

View Article Online
View Journal | View Issue

Check for updates

Cite this: *Mater. Adv.*, 2025, 6, 4037

In situ polymerized porous $Ti_3C_2T_x$/PANI as an electrode material for enhanced desalination performance in asymmetric capacitive deionization†

Xiaoyan Yang, *[ab] Xiaoke Lv,[a] Tao Wen,[a] Zhen Wang,[a] Yubin Zhou,[a] Tianmeng Zhang[c] and Jianfeng Zhang *[b]

Received 11th February 2025,
Accepted 30th April 2025

DOI: 10.1039/d5ma00123d

rsc.li/materials-advances

Capacitive deionization (CDI) has emerged as a sustainable technology for water desalination due to its low energy consumption and environmental compatibility. MXenes are promising CDI electrode materials owing to their hydrophilicity, metallic conductivity, and surface redox activity. However, the strong interlayer van der Waals forces between $Ti_3C_2T_x$ layers lead to severe self-restacking, thus decreasing the desalination performance. Herein, a porous $Ti_3C_2T_x$/polyaniline (PANI) composite material synthesized through *in situ* polymerization achieves a remarkable salt adsorption capacity (SAC) of 32.06 mg g^{-1} in 500 mg L^{-1} NaCl solution, surpassing pristine $Ti_3C_2T_x$ by 78%. Polyaniline can effectively reduce the self-stacking effect of $Ti_3C_2T_x$, increase its exposed active sites, and improve the stability and conductivity of $Ti_3C_2T_x$ through the addition of polyaniline, thereby enhancing its salt adsorption capacity and rate in capacitive deionization technology. This work provides a rational design strategy for MXene-based composites toward high-performance CDI systems.

1. Introduction

With more and more people facing fresh water scarcity globally, sustainable desalination technologies are urgently needed to alleviate water stress. Capacitive deionization (CDI) has emerged as a sustainable and energy-efficient alternative to conventional methods for brackish water treatment owing to its low operational voltage, environmental compatibility, and adaptability to intermittent renewable energy sources.[1–3] The electrode is the key component of a capacitive deionization system, which should have a large specific surface area, high electrical conductivity, excellent chemical stability and hydrophilicity.[4–7] The adsorption capacity of commonly used carbon electrode materials mainly depends on their specific surface area and pore structure, which results in limited adsorption capacity in solution and low purification efficiency.[2,8] Lee *et al.* first used the Faraday material $Na_4Mn_9O_{18}$ as an electrode in a hydride CDI system to improve the ion removal ability in 2014, which exhibited a 31.2 mg g^{-1} salt adsorption capacity,[9] then more scholars have conducted more in-depth research on the application of Faraday materials in capacitive deionization technology.

MXenes, typical Faraday materials, are promising CDI electrode materials owing to their hydrophilicity, metallic conductivity, and surface redox activity.[10–12] Srimuk *et al.* used $Ti_3C_2T_x$ as an electrode in a CDI system, which achieved a salt adsorption capacity of 13 mg g^{-1}.[13] The strong interlayer van der Waals forces between $Ti_3C_2T_x$ layers lead to severe self-restacking, dramatically reducing accessible ion adsorption sites. Moreover, the susceptibility to oxidative degradation in aqueous environments compromises long-term cycling stability. To prevent MXene layer stacking and improve electrochemical performance, some interlayer substances can be inserted, such as transition metal oxides,[14,15] nanoparticles,[16,17] *etc.* Xu *et al.* prepared a $Ti_3C_2T_x$/reduced graphene oxide (rGO) superlattice heterostructure to alleviate the self-stacking problem and increase the ion diffusion rate, achieving a Na^+ adsorption capacity of 48 mg g^{-1} with excellent long-term cycling performance.[18] Gong *et al.* synthesized bismuthene nanosheets (Bi-ene NSs)@MXene to facilitate ion and electron transport and provide abundant active sites, and a desalination capacity of 88.2 mg g^{-1} was achieved at 1.2 V.[19] Chen *et al.* prepared a $NaTi_2(PO_4)_3$/MXene nanohybrid using an MXene to improve the electrical conductivity and enhance the sodium

[a] *Institute of Advanced Ceramic Material and Fiber, School of Materials Science and Engineering, Zhejiang Sci-Tech University, Hangzhou, 310018, China. E-mail: xiaoyan@zstu.edu.cn*
[b] *College of Materials Science and Engineering, Hohai University, Nanjing 210098, China. E-mail: jfzhang_sic@163.com*
[c] *College of Materials and Textile Engineering, Nanotechnology Research Institute, Jiaxing University, Jiaxing, Zhejiang 314001, China*

† Electronic supplementary information (ESI) available. See DOI: https://doi.org/10.1039/d5ma00123d

insertion ability.[20] The capacitive deionization capability could be effectively enhanced by reducing the stacking of MXene layers.

Conductive polymers also have demonstrated potential in modifying MXenes through π–π interactions and hydrogen bonding.[21,22] Polyaniline is an excellent conductive polymer with many amine and imine functional groups on its surface, good environmental stability, and high pseudocapacitance, and can effectively improve the salt adsorption capacity in capacitive deionization.[23–25] Hussain *et al.* mixed activated carbon with PANI and MnO_2 to enhance the desalination performance, which showed a maximum SAC of 10.05 mg g^{-1}.[26] Wang *et al.* synthesized polypyrrole/polyaniline–carbon nanotube composites by *in situ* chemical oxidation polymerization, which achieved a SAC of 197.8 mg NaCl per g.[27] Ma *et al*. prepared a cobalt hexacyanoferrate/polyaniline composite with a hollow hierarchical tubular structure, which exhibited a salt adsorption capacity of 30.48 mg g^{-1}.[28] Therefore, combining PANI with an MXene to construct a porous structure can effectively reduce the stacking of MXene layers and improve the capacitive deionization performance. Li *et al*. fabricated MXene/PANI materials through hydrothermal reactions to accelerate the charge transfer and provide significant paths for ion insertion/extraction.[29] Lu *et al.* proposed a novel fluorine-selective composite electrode, MS-$Ti_3C_2T_x$/PANI/AC, which can effectively reduce F^- to 0.94 mg L^{-1}.[30] Despite previous efforts, the combination of PANI with MXenes *via in situ* polymerization for enhanced desalination remains unexplored.

Herein, *in situ* polymerization was used to form porous $Ti_3C_2T_x$/polyaniline. Phytic acid was used as a dopant, and the phosphate groups in phytic acid combined with the protonated nitrogen in polyaniline to crosslink multiple polymer chains to form the $Ti_3C_2T_x$/PANI material with a porous structure. Polyaniline can effectively reduce the self-stacking of $Ti_3C_2T_x$, increase the exposed active sites, and improve the stability, thereby enhancing the salt adsorption capacity and rate in capacitive deionization technology. This work establishes a new paradigm for developing robust MXene-based hybrid electrodes in desalination applications.

2. Experimental section

2.1 Materials

Hydrochloric acid (HCl), ammonium persulfate ($(NH_4)_2S_2O_8$), lithium fluoride (LiF) and other chemical reagents were obtained from Sinopharm Chemical Reagent Co., Ltd (Shanghai, China). Carbon black was obtained from Nanjing XFNANO Materials Tech Co., Ltd (Nanjing, China).

2.2 Synthesis of $Ti_3C_2T_x$/PANI

The $Ti_3C_2T_x$ dispersion solution was obtained according to the reported work.[31,32] 0.572 g of ammonium persulfate was dissolved in 2 mL of deionized aqueous solution, and the mixture was denoted as solution A. 0.414 mL of phytic acid (70 wt%) was added into to 0.916 mL of aniline monomer, dispersed evenly, and then poured in $Ti_3C_2T_x$ dispersion, and the resulting mixture was denoted as solution B. Solution A and solution B were mixed slowly at 4 °C, the color of the solution changed from light brown to dark green after 3 min and a gel-like structure formed after 72 hours. Then the solution was purified with deionized water for 24 hours and finally freeze-dried to obtain the $Ti_3C_2T_x$/PANI material with a porous structure.

2.3 Materials characterization

The microscopic morphology of the materials was observed by using a HITACHI SU8220 scanning electron microscope (SEM) and a JEM-2100F transmission electron microscope (TEM). The phase composition of the materials was analyzed by using a D8 Advance from Bruker and an ESCALAB 250Xi System from Thermo Fisher. The pore size distribution and specific surface area of the materials were measured by using Quantachrome NovaWin. The electrochemical tests were conducted by using a CHI760E electrochemical workstation, and the electrical conductivity was tested by using a DDSJ-318. Detailed procedures for electrochemical testing and asymmetric capacitive deionization testing can be found in the ESI.†

3. Results and discussion

The schematic diagram of $Ti_3C_2T_x$/PANI synthesis is shown in Fig. 1. Due to the presence of van der Waals forces, the layers of $Ti_3C_2T_x$ are easily stacked together, which limits the storage space of ions during the capacitive deionization process. In order to reduce the stacking of $Ti_3C_2T_x$ sheets, phytic acid was used as a dopant and a gel agent to polymerize on the surface and between layers of $Ti_3C_2T_x$ to form polyaniline. During the polymerization process, each phytic acid molecule containing 6 phosphate groups could combine with protonated N on the polyaniline polymer chain and act as an anionic doping agent.[33] The absorption peak at 617 cm^{-1} (Fig. S1, ESI†) is a characteristic peak of P–O bending vibration, indicating the successful doping of phytic acid during the synthesis of polyaniline. At the same time, each phytic acid molecule can interact with more than one phospholipid chain to cross-link multiple polyaniline polymer chains, forming a porous structure containing nano- and micron-sized pores. In the SEM and TEM images of $Ti_3C_2T_x$ and $Ti_3C_2T_x$/PANI (Fig. 2), there are certain wrinkles on the surface of $Ti_3C_2T_x$ after ultrasonic treatment, showing a looser, few-layer structure, which helps to improve the hydrophilicity of $Ti_3C_2T_x$ and its dispersibility in aqueous solutions. $Ti_3C_2T_x$/PANI shows a porous structure formed by polymer cross-linking, with many nanopores or micropores stacked on the surface due to the cross-linking reaction between phytic acid molecules and polyaniline. More electron transport channels formed by *in situ* polymerization of polyaniline between the layers of $Ti_3C_2T_x$, expanding the ion transport pathway and accelerating the transport rate.

The structure of the material was characterized by XRD and FTIR, as shown in Fig. 3. Polyaniline exhibits weak characteristic peaks of (020) and (200) crystal planes at 2θ of 20.0° and

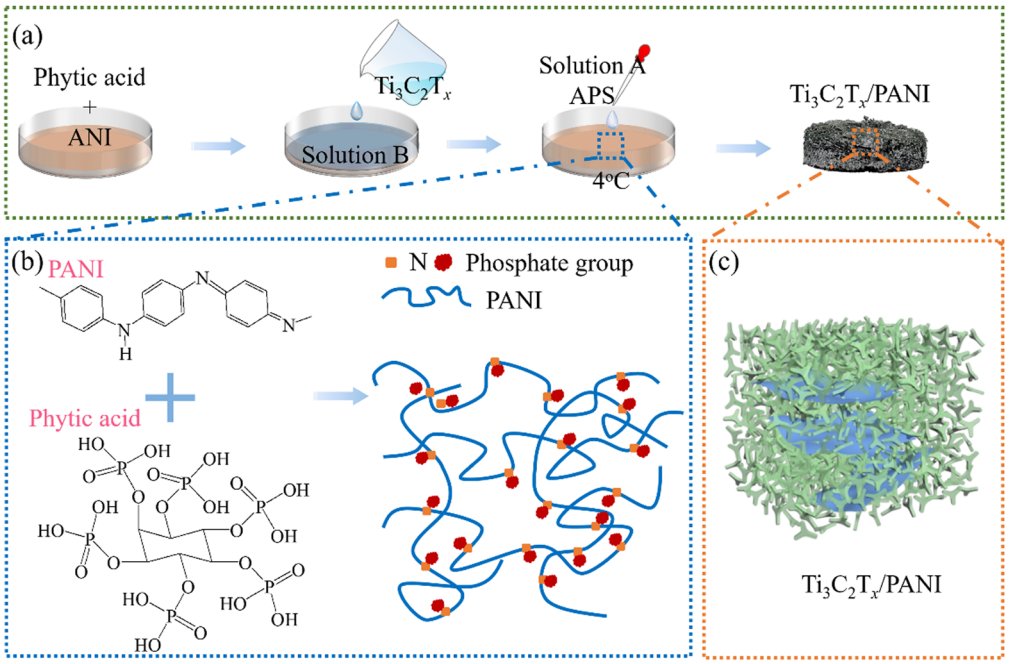

Fig. 1 The synthesis process of porous $Ti_3C_2T_x$/PANI powders. (a) The synthesis process of $Ti_3C_2T_x$/PANI. (b) The crosslinking process of phytic acid and PANI. (c) The structure diagram of $Ti_3C_2T_x$/PANI.

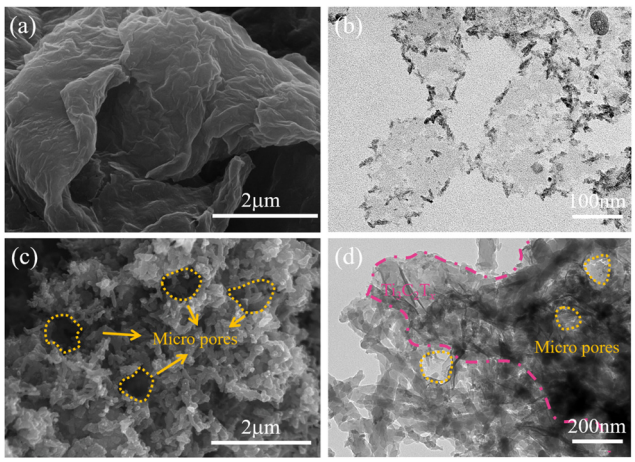

Fig. 2 The SEM and TEM images of different samples. (a) The SEM image of $Ti_3C_2T_x$, (b) the TEM image of $Ti_3C_2T_x$, and the (c) SEM and (d) TEM images of porous $Ti_3C_2T_x$/PANI.

25.2°, respectively. The $Ti_3C_2T_x$/PANI composite material exhibits characteristic peaks of the (002), (004) and (006) crystal planes of $Ti_3C_2T_x$ at 2θ of 5.98°, 18.9° and 27.4°. Compared with $Ti_3C_2T_x$, the characteristic peak of the (002) crystal plane shifted towards a small angle direction, from 13.1036 Å to 14.7675 Å, indicating that the interlayer space of $Ti_3C_2T_x$ is increased by 1.6639 Å, which may be due to the increase in the interlayer spacing of polyaniline. At the same time, the composite material $Ti_3C_2T_x$/PANI has strong characteristic peaks of (020) and (200) of polyaniline at 2θ of 20.0° and 25.2°. The FTIR curve of $Ti_3C_2T_x$ mainly consists of three characteristic peaks at 3431 cm^{-1}, 1618 cm^{-1}, and 1072 cm^{-1}, which are the stretching vibration peaks of O–H. The contraction vibration peak of double bonds and the vibration peak of carbon oxygen single bonds, indicating the presence of hydroxyl groups on the surface of $Ti_3C_2T_x$. There are four characteristic peaks in the FTIR spectrum of polyaniline at 1578 cm^{-1}, 1500 cm^{-1}, 1300 cm^{-1} and 1072 cm^{-1}, where those at 1578 cm^{-1} and 1500 cm^{-1} correspond to the C=C quinone ring and benzene ring, respectively. The peak at 1300 cm^{-1} represents the aromatic C–N bond and the peak at 1149 cm^{-1} represents the C–C skeleton vibrational peak. The phytic acid dopant exhibits quinone ring characteristic peaks in the FTIR spectrum of polyaniline, and the characteristic peak of P–O bending vibration at 613 cm^{-1} indicates the successful doping of phytic acid, effectively improving its conductivity. In $Ti_3C_2T_x$/PANI composite materials, there are mainly the stretching vibration peaks of O–H, the vibration peaks of C=C quinone and benzene rings, and the characteristic peaks of aromatic C–N bonds, which will improve the conductivity and accelerate the ion transfer rate as an electrode during the capacitive deionization process.[34]

Fig. 4 shows the XPS spectra of $Ti_3C_2T_x$ and $Ti_3C_2T_x$/PANI. Due to the liquid-phase etching of LiF and HCl, $Ti_3C_2T_x$ exhibits four characteristic peaks: F 1s, O 1s, Ti 2p, and C 1s, indicating that there are a certain number of fluorine and hydroxyl groups on the surface of $Ti_3C_2T_x$, which is beneficial for the adsorption of cations during capacitive deionization. The XPS pattern of the $Ti_3C_2T_x$/PANI composite material shows a characteristic peak of N 1s at 389 eV, which is attributed to the N element produced by the amine groups in polyaniline. Fig. 4(b) shows a detailed scan of the Ti element, including mainly four characteristic peaks of Ti–O $2p_{1/2}$, Ti–C $2p_{1/2}$, Ti–O

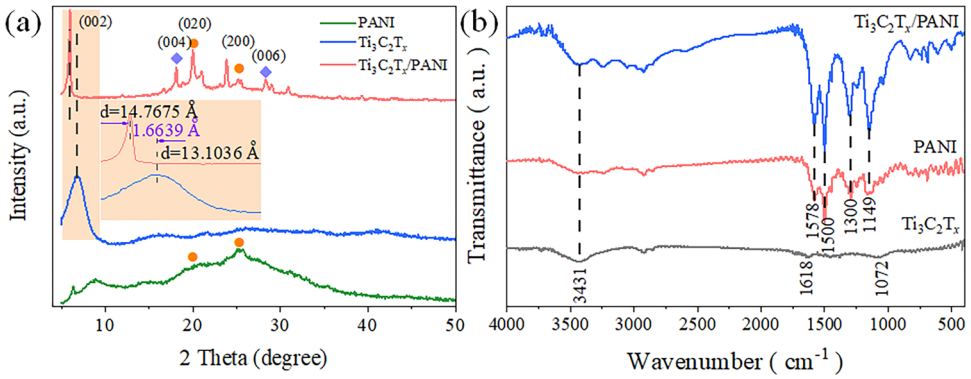

Fig. 3 The (a) XRD and (b) FTIR patterns of different samples.

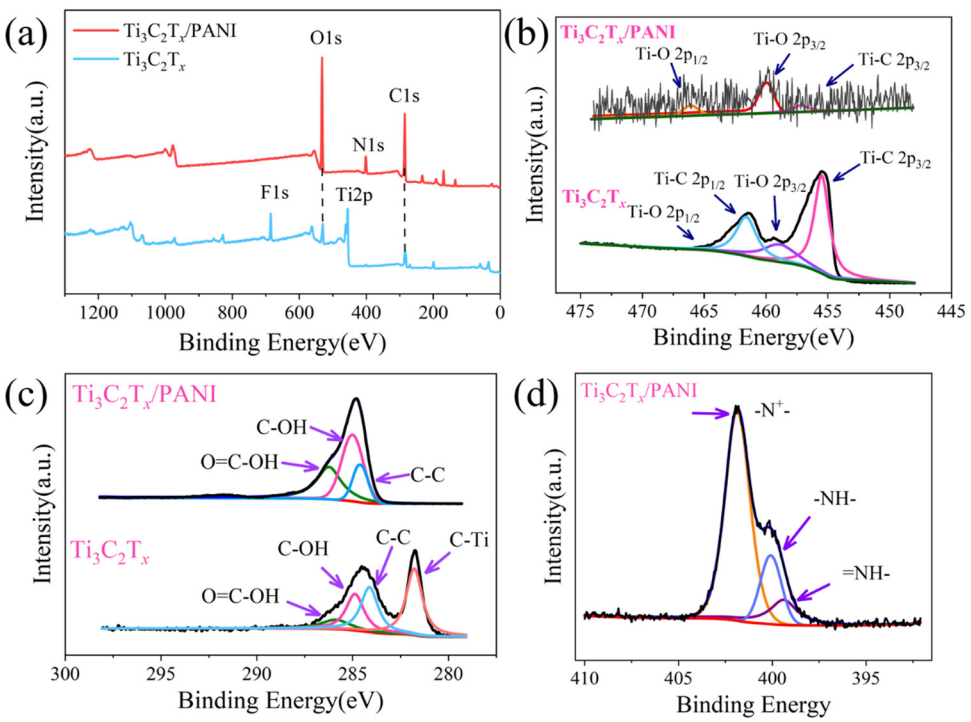

Fig. 4 The XPS spectra of $Ti_3C_2T_x$ and $Ti_3C_2T_x$/PANI. (a) The survey spectra of $Ti_3C_2T_x$ and $Ti_3C_2T_x$/PANI and the high resolution XPS spectra of (b) Ti 2p, (c) C 1s and (d) N 1s for $Ti_3C_2T_x$ and $Ti_3C_2T_x$/PANI.

$2p_{3/2}$, and Ti–C $2p_{3/2}$, located at 465.0 eV, 461.0 eV, 456.4 eV, and 455.1 eV, respectively. For the $Ti_3C_2T_x$/PANI composite material, the peak intensities of Ti–C $2p_{1/2}$ and Ti–C $2p_{3/2}$ decrease, and those of Ti–O $2p_{3/2}$ and Ti–O $2p_{1/2}$ increase, and this may be attributed to the increase of polyaniline, due to which the characteristic peaks of Ti–C bonds are not detected. In the figure of element C, $Ti_3C_2T_x$ exhibits four characteristic peaks of O═C–OH, C–OH, C–C, and C–Ti, located at 285.9 eV, 284.1 eV, 284.0 eV, and 281.8 eV, respectively. However, the intensity of the characteristic peak of C–Ti decreases and that of the C–C characteristic peak increases in the $Ti_3C_2T_x$/PANI composite material, which is due to the presence of more C–C bonds in polyaniline. Fig. 4(d) shows the N element spectrum of the $Ti_3C_2T_x$/PANI composite material, with three main characteristic peaks corresponding to quinone imine (═N–), phenylimine (–NH–), and cationic nitrogen atoms ($–N^+–$) at 398.0 eV, 399.5 eV, and 401.2 eV, respectively.

To confirm the specific surface area of $Ti_3C_2T_x$ and $Ti_3C_2T_x$/PANI composite materials, nitrogen adsorption–desorption curve testing and Barrett–Joyner–Halenda pore size distribution analysis were performed, as shown in Fig. S2 and Table S1 (ESI†). The hysteresis loop of $Ti_3C_2T_x$ mainly exists in the medium pressure section, which may be due to the narrow pores formed by layered materials, consistent with the morphology in Fig. 2. Due to the van der Waals forces, it is prone to agglomeration between the layers, resulting in the formation of some narrow pores. The specific surface area of $Ti_3C_2T_x$ is

approximately 13.53 $m^2 g^{-1}$ after calculation. The hysteresis loop of the $Ti_3C_2T_x$/PANI composite material is distributed in the medium- and high-pressure region, which is formed by the stacking of layered particles and narrow pores, which can exist as a network structure of polyaniline and stacked $Ti_3C_2T_x$. The specific surface area of the $Ti_3C_2T_x$/PANI composite material is about 17.76 $m^2 g^{-1}$ after calculation, slightly higher than that of $Ti_3C_2T_x$. The average pore size of $Ti_3C_2T_x$ in Fig. S2 (ESI†) is about 9.03 nm, with a wide distribution range (2–70 nm), but mainly concentrated at around 3.53 nm, with a pore volume of approximately 0.031 $cm^3 g^{-1}$. The pore size distribution of the $Ti_3C_2T_x$/PANI composite material is relatively concentrated, ranging from 2 to 20 nm, with a higher content in the range of 2 to 8 nm. The average pore size is about 9.22 nm, and the pore volume is about 0.041 $cm^3 g^{-1}$, slightly higher than the average pore size and volume of $Ti_3C_2T_x$. This may be due to the formation of the three-dimensional network structure of cross-linked polyaniline, which increases the number of nanopores and micrometer pores to a certain extent, and leads to concentrated pore size distribution, causing a slight increase in the interlayer spacing of $Ti_3C_2T_x$. As a result, the specific surface area of the $Ti_3C_2T_x$/PANI composite material is slightly increased, and its use as an electrode in capacitive deionization technology can provide more storage space for ions.

The electrochemical performance of $Ti_3C_2T_x$ in 1 M NaCl solution was studied, and the results are shown in Fig. S3 (ESI†). Firstly, different scanning rates (50–500 mV s^{-1}) were used to obtain the corresponding cyclic voltammetry curves. As the scanning rate increases, the enclosed area of the curve increases, but the overall morphology remains unchanged, indicating that the $Ti_3C_2T_x$ electrode can still maintain certain stability at high scanning rates without any changes in the electrode material structure or phase. Fig. S3(b) (ESI†) shows the galvanostatic charge–discharge (GCD) curves at different current densities (0.5–2.0 A g^{-1}), which exhibit an overall ''isosceles triangle'' structure, indicating the charge discharge reversibility of the electrode material in NaCl solution. After calculation, the maximum specific capacity of the $Ti_3C_2T_x$ electrode is about 61.7 F g^{-1}. After fitting calculation, the charge transfer resistance of $Ti_3C_2T_x$ in NaCl solution is approximately 2195 Ω, and the internal resistance reached 2.85 Ω, which limits the charge transfer rate and reduces the ion transport speed.

The electrochemical performance of the $Ti_3C_2T_x$/PANI composite material in 1 M NaCl solution is shown in Fig. S4 (ESI†). Fig. S4(a) (ESI†) shows the CV curves at different scan rates ranging from 10 mV s^{-1} to 200 mV s^{-1}, which no longer exhibit a rectangular shape as a whole and remain unchanged at different scan rates. The porous structure formed by polyaniline and $Ti_3C_2T_x$ provides more storage space for ions. At the same time, Na^+ may enter the interlayer or embed into the active sites of polyaniline, thereby promoting the generation of some pseudocapacitance and improving the ion storage capacity. The internal resistance of the $Ti_3C_2T_x$/PANI electrode material is almost unchanged compared to the $Ti_3C_2T_x$ electrode material, indicating that the synthesis of polyaniline did not increase the internal resistance of the electrode material and did not reduce the rate of charge transfer inside the electrode material. The internal resistance of the $Ti_3C_2T_x$/PANI electrode is about 2.92 Ω, which is almost unchanged compared to the $Ti_3C_2T_x$ electrode material, indicating that the synthesis of polyaniline does not increase the internal resistance of the electrode material. After fitting calculation, the charge transfer resistance of the $Ti_3C_2T_x$/PANI electrode is 343.4 Ω, which is much lower than that of $Ti_3C_2T_x$, indicating that electrons can pass through the electrode–electrolyte interface more quickly and improve ion adsorption efficiency.

The internal resistance of the $Ti_3C_2T_x$/PANI electrode is about 2.92 Ω, which shows almost no increase compared with the $Ti_3C_2T_x$ electrode material, indicating that the synthesis of polyaniline does not increase the internal resistance of the electrode material and does not reduce the charge transfer rate inside the electrode material.

The desalination performance of the electrode was investigated using asymmetric capacitive deionization, and the variation of the conductivity of NaCl solution with an initial concentration of 500 mg L^{-1} at a flow rate of 10 mL min^{-1} and a voltage of 1.2 V, as shown in Fig. S4 (ESI†). The rate of decrease in solution conductivity slowly reaches equilibrium in nearly 50 minutes for the $Ti_3C_2T_x$ electrode, and the final adsorption capacity of Na^+ is about 14.75 mg g^{-1}. But for the $Ti_3C_2T_x$/PANI electrode, the conductivity decreases rapidly in the first 10 minutes, and the adsorption capacity is about 32.06 mg g^{-1} after calculation. Fig. S5(b) (ESI†) shows the corresponding Ragone plot, which more intuitively reflects the relationship between the salt adsorption capacity and salt adsorption rate of these two electrode materials. The stacking of $Ti_3C_2T_x$ layers prevents ions from entering the interior of the electrode material, thereby affecting the salt adsorption rate. The adsorption rate of the $Ti_3C_2T_x$/PANI material is relatively fast at the initial stage, gradually decreasing and approaching adsorption saturation. This is because the cross-linked PANI provides more transport paths for ions, improving the transport rate of ions inside the electrode and accelerating the salt adsorption rate. And the porous structure reduces the stacking of $Ti_3C_2T_x$ layers, exposing more active sites and increasing the overall salt adsorption capacity of the electrode material.

Fig. 5(a) and (b) shows the desalination performance and Ragone curves at different initial salt concentrations of the $Ti_3C_2T_x$/PANI electrode. The Na^+ adsorption capacity reaches the maximum of 33.65 mg g^{-1} in 500 mg L^{-1} NaCl solution. The Ragone curves for initial salt concentrations ranging from 100 mg L^{-1} to 300 mg L^{-1} are relatively similar, while the salt adsorption rates are higher at 400 mg L^{-1} and 500 mg L^{-1}. This is because, as the salt concentration increases, the conductivity of NaCl solution also increases, thereby promoting the transport of ions from the solution to the surface or interior of the electrode to increase the salt adsorption capacity and the ion adsorption rate. At the same time, the porous structure formed by polyaniline provides more transport pathways for ions, which can effectively accelerate the adsorption of ions in salt solutions by electrode materials. Subsequently, the adsorption

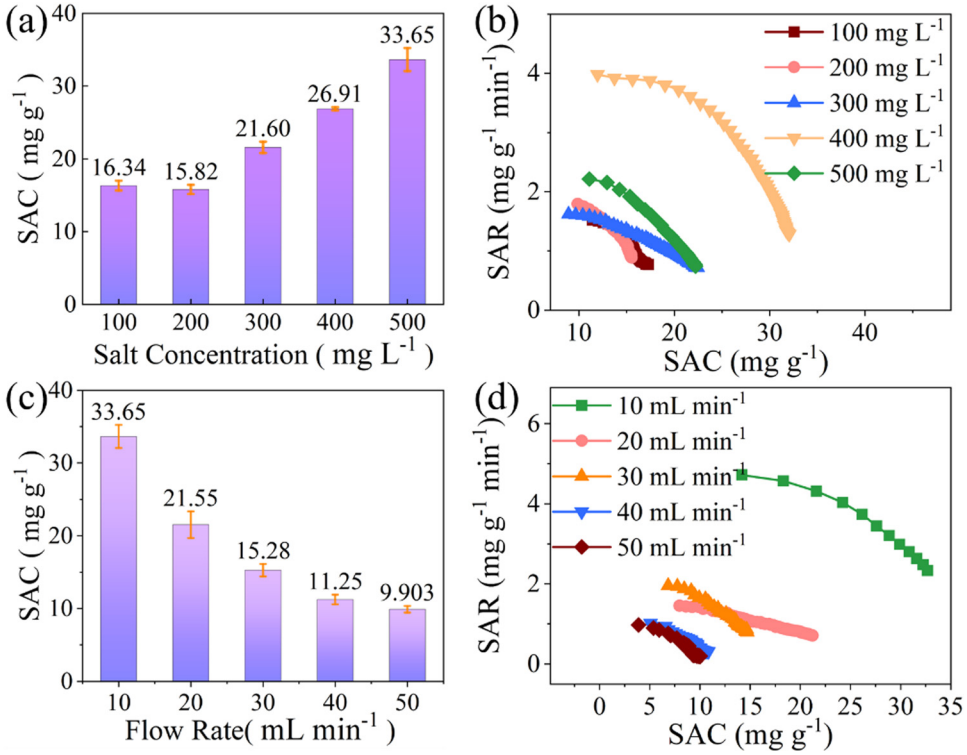

Fig. 5 (a) The plot of salt adsorption concentration and (b) the Ragone curve for $Ti_3C_2T_x$/PANI at different NaCl concentrations at 1.2 V and 10 mL^{-1} min^{-1}. (c) The plot of salt adsorption concentration and (d) the Ragone curve for $Ti_3C_2T_x$/PANI by different flow rates at 500 mg L^{-1} NaCl concentration at 1.2 V.

capacity of $Ti_3C_2T_x$/PANI was tested at different flow rates, as shown in Fig. 5(c) and (d). As the flow rate increases from 10 mL min^{-1} to 50 mL min^{-1}, the salt adsorption capacity of the electrode decreases. At flow rates of 10 mL min^{-1}, 20 mL min^{-1}, 30 mL min^{-1}, 40 mL min^{-1}, and 50 mL min^{-1}, the salt adsorption capacities were 33.65 mg g^{-1}, 21.55 mg g^{-1}, 15.28 mg g^{-1}, 11.25 mg g^{-1}, and 9.90 mg g^{-1}, respectively. When the solution flow rate reaches 40 mL min^{-1} or above, the salt adsorption capacity remains at around 10 mg g^{-1}, with a decrease in magnitude. In the Ragone plot, the curve is located in the upper right corner of the plot at a flow rate of 10 mL min^{-1}, indicating a higher salt adsorption capacity and rate. This may be due to the ions in the solution having sufficient time to come into contact with the electrode material, thereby promoting the complete embedding of ions into the active sites of the electrode material or adsorption into the pore size of the electrode material. As the flow rate increases, the curve gradually shifts towards the lower left corner of the plot, indicating a decrease in the salt adsorption capacity and rate.

A comparison of the electrode material $Ti_3C_2T_x$/PANI in this article with other reference materials is shown in Fig. 6 (specific values are shown in Tables S2 and S3, ESI†). Fig. 6(a) presents a radar chart comparing the $Ti_3C_2T_x$/PANI with PANI-based electrodes across three critical performance metrics: salt adsorption

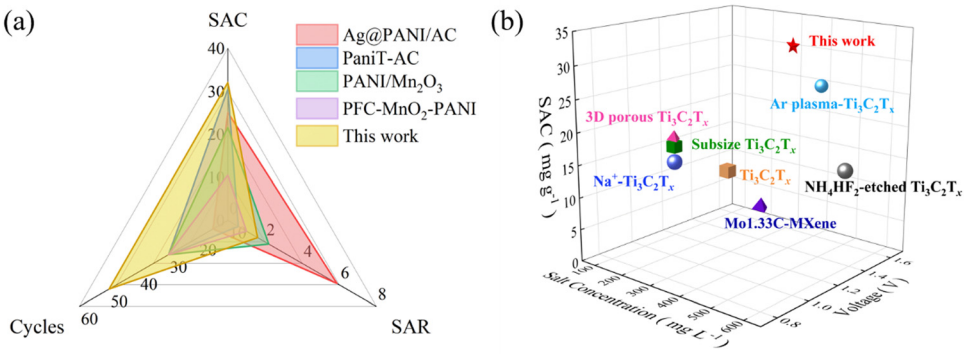

Fig. 6 Comparison of the adsorption performance of $Ti_3C_2T_x$/PANI with (a) different PANI related materials and (b) $Ti_3C_2T_x$ materials (the exact values and references are listed in Tables S2 and S3, ESI.†)

capacity (SAC), salt adsorption rate (SAR) and cycle stability. Each material is represented by a distinct color-coded polygon, where the enclosed area quantitatively reflects the overall desalination performance. The $Ti_3C_2T_x$/PANI electrode (yellow polygon) exhibits the largest enclosed area, surpassing all counterparts. Fig. 6(b) shows the performance comparison between different MXene materials and the $Ti_3C_2T_x$/PANI electrode material prepared in this paper, mainly comparing the salt adsorption capacity at different voltages and initial concentrations. Compared to the MXene material in the literature, the SAC of the $Ti_3C_2T_x$/PANI electrode material is relatively high, which may be attributed to the porous structure providing more storage space for ion adsorption. Finally, the cycling stability of the $Ti_3C_2T_x$/PANI electrode material was tested over 50 cycles, and the results are shown in Fig. S6 (ESI†). The SAC gradually decreases with the increase of the cycle number. After 20 cycles of adsorption/desorption, the SAC stabilizes at about 60% of its initial value. The decrease in salt adsorption capacity is mainly attributed to the relatively poor stability of the Faraday material polyaniline and $Ti_3C_2T_x$. During the capacitive deionization process, Na^+ will be embedded into the pores of the $Ti_3C_2T_x$/PANI electrode, and after multiple cycles, Na^+ may not be able to escape from the pores, reducing the active sites on the surface and interior of the material, resulting in a decrease in the cycling performance of the electrode material.[32,35]

To analyze the capacitive deionization adsorption mechanism of the $Ti_3C_2T_x$/PANI electrode material, the adsorption conditions at different adsorption concentrations were fitted with pseudo first and second order kinetics, as shown in Fig. 7 and Table S4 (ESI†). The fitting regression constant R^2 of the pseudo first order kinetics curve is basically around 0.92. With the increase of solution concentration, the fitting regression constant of pseudo first order kinetics gradually increases, which may be due to the increase of solution concentration and the improvement of its own conductivity, making the ion transport in the solution more uniform and faster, thereby improving the adsorption performance of the electrode material. The adsorption plot in the actual experiment is closer to the fitted line when the initial concentration ranges from 100 mg L^{-1} to 500 mg L^{-1} in the fitting graph of pseudo second order kinetics, and the actual adsorption of surface ions is more consistent with the fitted situation. The regression constant R^2 in Table S4 (ESI†) remains above 0.99, which is closer to 1. Among them, at 400 mg L^{-1} and 500 mg L^{-1}, the R^2 value is relatively higher and the fitting is better. This may also be due to the increased conductivity of the solution, which accelerates the adsorption rate of ions and makes the adsorption process more stable. Comparing the curve fitting of two adsorption kinetics models, it can be found that the fitting of pseudo second order kinetics is more suitable for the actual adsorption of $Ti_3C_2T_x$/PANI electrode materials.

Fig. 7(c) shows a diagram of the adsorption mechanism of the asymmetric capacitive deionization process. When a forward voltage is applied, sodium ions and chloride ions move towards both sides of the electrode, adsorbing onto the surface and interior of the electrode, reducing the concentration of the solution and achieving the purpose of desalination. The adsorption mechanism of the activated carbon electrode, which is mainly based on the double layer capacitance adsorption principle, depends on the specific surface area and pore structure of the activated carbon electrode. During the process of applying voltage, the electrode material forms a double layer

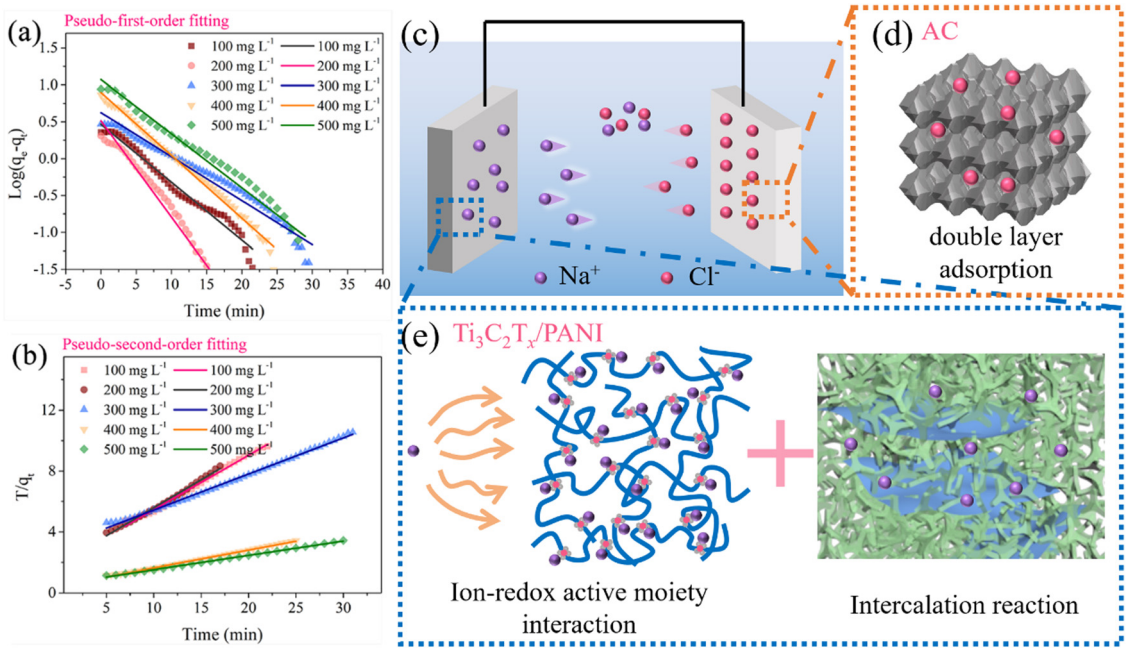

Fig. 7 (a) Pseudo first order and (b) pseudo second order kinetic fitting curves of the adsorption properties of the $Ti_3C_2T_x$/PANI electrode material at different concentrations. (c) The adsorption process of capacitive deionization for the $Ti_3C_2T_x$/PANI electrode. (d) The EDLC ion storage of the AC electrode. (e) The ion intercalation storage process of the $Ti_3C_2T_x$/PANI electrode.

on the surface of the activated carbon electrode, thereby achieving the purpose of ion adsorption. For the $Ti_3C_2T_x$/PANI electrode material, which is composed of the Faraday material, ions have active site embedding and adsorption mechanisms, as shown in Fig. 7(c). There are certain active sites on the surface of the conductive polymer polyaniline. During the application of voltage, ions will be embedded into the active sites, thereby achieving ion adsorption. At the same time, during the adsorption process, sodium ions will be embedded into the middle of $Ti_3C_2T_x$ layers, increasing the interlayer distance and thus improving the adsorption capacity of the electrode material. Under the combined action of polyaniline and $Ti_3C_2T_x$, the overall adsorption capacity of the electrode material is improved. At the same time, phytic acid as a dopant and binder promotes the formation of a conductive network of polyaniline, providing more pathways for ion transport, thereby accelerating the ion transport speed and improving the salt adsorption rate of electrode materials. By designing the microstructure of electrode materials, the salt adsorption capacity and rate of electrode materials can be effectively improved.

4. Conclusion

Porous $Ti_3C_2T_x$/PANI was synthesized through a simple polymerization method, which used phytic acid as a dopant and binder to combine the conductive polyaniline and $Ti_3C_2T_x$. The phosphate groups in phytic acid molecules combine with protonated N on polyaniline polymer chains to achieve anion doping. At the same time, phytic acid molecules interact with phospholipid chains to crosslink multiple polyaniline polymer chains to form the porous structure. The addition of conductive polyaniline provides more pathways for ion movement between $Ti_3C_2T_x$ layers, thereby improving the ion transport efficiency. The desalination performance of composite materials was tested in an asymmetric capacitive deionization system, and the salt adsorption capacity reached 32.06 mg g^{-1}, and after 50 cycles of performance testing, the capacity remained above 60%.

Data availability

All relevant data are within the manuscript and its ESI.†

Conflicts of interest

There are no conflicts to declare.

Acknowledgements

This research was supported by Zhejiang Provincial Natural Science Foundation of China (Grant No. LQ24E020002) and the Science Foundation of Zhejiang Sci-Tech University (ZSTU) (Grant No. 22212247-Y).

References

1 J. W. Blair and G. W. Murphy, *Saline Water Conversion*, American Chemical Society, 1960, ch. 20, vol. 27, pp. 206–223.
2 A.-H. Feng, Y. Yu and L.-X. Song, *J. Inorg. Mater.*, 2016, **31**, 123–134.
3 J. Ma, L. Chen and F. Yu, *Sep. Purif. Technol.*, 2024, **335**, 126095.
4 H. Wang, D. Wei, H. Gang, Y. He, H. Deng, L. Hou, Y. Shi, S. Wang, W. Yang and L. Zhang, *ACS Sustainable Chem. Eng.*, 2019, **8**, 1129–1136.
5 Y. He, L. Huang, Y. Zhao, W. Yang, T. Hao, B. Wu, H. Deng, D. Wei, H. Wang and J. Luo, *Environ. Sci.: Nano*, 2020, **7**, 3007–3019.
6 H. Li, S. Dai, Y. Wu, Q. Dong, J. Chen, H.-Y. T. Chen, A. Hu, J.-P. Chou and T.-Y. Chen, *Adv. Sci.*, 2023, **10**, 2207109.
7 S. Kumar, N. M. Aldaqqa, E. Alhseinat and D. Shetty, *Angew. Chem., Int. Ed.*, 2023, **62**, e202302180.
8 P. Liu, L. Shi, H. S. Park, X. Chen, Z. Zhao and D. Zhang, *J. Mater. Chem. A*, 2017, **5**, 13907–13943.
9 J. Lee, S. Kim, C. Kim and J. Yoon, *Energy Environ. Sci.*, 2014, **7**, 3683–3689.
10 B. Chen, A. Feng, R. Deng, K. Liu, Y. Yu and L. Song, *ACS Appl. Mater. Interfaces*, 2020, **12**, 13750–13758.
11 B. Chen, A. Feng, K. Liu, J. Wu, Y. Yu and L. Song, *Ceram. Int.*, 2021, **47**, 3665–3670.
12 P. Dubey, *ChemistrySelect*, 2023, **8**, e202302281.
13 P. Srimuk, F. Kaasik, B. Krüner, A. Tolosa, S. Fleischmann, N. Jäckel, M. C. Tekeli, M. Aslan, M. E. Suss and V. Presser, *J. Mater. Chem. A*, 2016, **4**, 18265–18271.
14 Z. Sun, H. Xu, J. Fu, H. Bai, Y. Qiao, P. Liu, Y. Li, Y. Jiang, B. Hou and Y. Wang, *Sep. Purif. Technol.*, 2024, **347**, 127520.
15 W. Xi, J. Jin, Y. Zhang, R. Wang, Y. Gong, B. He and H. Wang, *Nanoscale*, 2022, **14**, 11923–11944.
16 Y. Zhang, H. Li, Q. Yang, S. Zhang, B. Zhao, J. Wu, N. Shang, X. Zhao, Z. Xiao, X. Zang, J. Kim, X. Xu and Y. Yamauchi, *J. Mater. Chem. A*, 2023, **11**, 14356–14365.
17 Y. Zhang, J. Zhou, D. Wang, R. Cao and J. Li, *Chem. Eng. J.*, 2022, **430**, 132702.
18 H. Xu, M. Li, S. Gong, F. Zhao, Y. Zhao, C. Li, J. Qi, Z. Wang, H. Wang, X. Fan, W. Peng and J. Liu, *J. Colloid Interface Sci.*, 2022, **624**, 233–241.
19 S. Gong, H. Liu, F. Zhao, Y. Zhang, H. Xu, M. Li, J. Qi, H. Wang, C. Li, W. Peng, X. Fan and J. Liu, *ACS Nano*, 2023, **17**, 4843–4853.
20 Z. Chen, X. Xu, Z. Ding, K. Wang, X. Sun, T. Lu, M. Konarova, M. Eguchi, J. G. Shapter, L. Pan and Y. Yamauchi, *Chem. Eng. J.*, 2021, **407**, 127148.
21 L. Zhang, Y. Cai, R. Fang, Y. Wang and S. Xu, *Sep. Purif. Technol.*, 2024, **337**, 126362.
22 Y. Cai, Y. Wang, R. Fang and J. Wang, *Sep. Purif. Technol.*, 2022, **280**, 119828.
23 J. Guo, Y. Wang, H. Zhang, Y. Cai and R. Fang, *Desalination*, 2023, **548**, 116305.
24 F. Yu, L. Wang, Y. Wang, X. Shen, Y. Cheng and J. Ma, *J. Mater. Chem. A*, 2019, **7**, 15999–16027.

25 W. Shi, X. Liu, T. Deng, S. Huang, M. Ding, X. Miao, C. Zhu, Y. Zhu, W. Liu, F. Wu, C. Gao, S. W. Yang, H. Y. Yang, J. Shen and X. Cao, *Adv. Mater.*, 2020, **32**, 1907404.
26 H. Hussain, A. Jilani, N. Salah, A. Memić, M. O. Ansari and A. Alshahrie, *Water Environ. Res.*, 2024, **96**, e11038.
27 Y. Wang, R. Wang, S. Xu, Q. Liu and J. Wang, *Desalin. Water Treat.*, 2015, **54**, 3248–3256.
28 D. Ma, X. Xue, M. Niu, Y. Wang, Q. Luo, X. Zhu, H. Li and D. Wang, *Sep. Purif. Technol.*, 2024, **348**, 127804.
29 Y. Li, P. Kamdem and X.-J. Jin, *J. Alloys Compd.*, 2021, **850**, 156608.
30 Z. Lu, D. Zhang, H. Kang, S. Guo, H. Ge, Y. Li, Z. Wang and Y. Li, *Chem. Eng. J.*, 2024, **497**, 154664.
31 X. Yang, H. Jiang, W. Zhang, T. Liu, J. Bai, F. Guo, Y. Yang, Z. Wang and J. Zhang, *Sep. Purif. Technol.*, 2021, **276**, 119379.
32 X. Yang, Z. Jia, W. Zhang, G. Ying, Z. Wang, Z. Lu and J. Zhang, *Desalination*, 2022, **535**, 115816.
33 K. A. Milakin, Z. Morávková, U. Acharya, M. Kašparová, S. Breitenbach, O. Taboubi, J. Hodan, J. Hromádková, C. Unterweger, P. Humpolíček and P. Bober, *Polymer*, 2021, **217**, 123450.
34 S. Tian, Z. Zhang, X. Zhang and K. Ostrikov, *J. Colloid Interface Sci.*, 2019, **537**, 247–255.
35 Y. Ren, M. Liang, Z. Zhou, X. Zhang, F. Yu, X.-G. Li and J. Ma, *Adv. Funct. Mater.*, 2025, 2502601.